Apatite and fluorite control the transport of tungsten in calcium-bearing hydrothermal fluids

Xin-Song Wang [a], A.E. Williams-Jones [b], Rui-Zhong Hu [a], Zi-Qi Jiang [a], Lin-Bo Shang [a], Xian-Wu Bi [a,*]

[a] State Key Laboratory of Ore Deposits Geochemistry, Institute of Geochemistry, Chinese Academy of Sciences, Guiyang 550081, China
[b] Department of Earth and Planetary Sciences, McGill University, 3450 University Street, Montreal, QC H3A 0E8, Canada

ARTICLE INFO

ABSTRACT

Minerals associated with ores (gangue minerals) record the physicochemical conditions of ore-forming fluids. Whether and/or how they affect the solubility of ore minerals, however, is rarely evaluated. Here, we present results of an experimental study of the solubility of scheelite (responsible for >70% of the global supply of tungsten). They show that phosphate and fluoride sequester calcium from scheelite to form apatite and/or fluorite. These gangue minerals, which are common in tungsten deposits, vary in abundance depending on pH and the phosphorus/fluorine content of the fluid. Because of their precipitation, scheelite dissolution releases hundreds of ppm of tungsten to the fluid, especially at near neutral pH. This suggests that the presence of phosphorus/fluorine in a tungsten-bearing hydrothermal fluid may prevent the deposition of scheelite due to the formation of apatite/fluorite, or lead to the dissolution of scheelite and, in turn, enrich the fluid in tungsten. Models based on our data show that magmatic-hydrothermal phosphorus- and fluorine-rich fluids are enriched in tungsten by a factor of up to 220 during high-temperature alteration, and form high-grade deposits of ferberite on cooling, or of scheelite because of their interaction with calcium-enriched rocks. Thus, the concentration of fluorine and phosphorus, as well as pH, are key factors affecting the transport and deposition of tungsten in calcium-bearing hydrothermal systems that, if they act synergistically, can efficiently remobilize early low-grade tungsten mineralization and enrich the ore-forming fluids in tungsten, leading to the formation of giant deposits. Such competition between ore and gangue minerals for components of the mineralizing fluid is also probably a feature of hydrothermal systems involving other metals and should be considered in future studies of the genesis of the corresponding ores.

© 2023 Elsevier Ltd. All rights reserved.

1. Introduction

Gangue minerals play an important role in studies of hydrothermal metallic mineral deposit genesis by providing essential information on the physicochemical conditions of ore formation (Hedenquist and Lowenstern, 1994; Audétat et al., 1998; Ulrich et al., 1999; Seward et al., 2014). This information helps in predicting the solubility of ore minerals and the aqueous speciation of the corresponding metals, in turn, enabling the construction of robust models of hydrothermal ore genesis (Heinrich, 1990; Williams-Jones and Migdisov, 2014; Brugger et al., 2016). A fact that is generally ignored, however, is that ore mineral solubility may be controlled by the competition of the gangue minerals for some of the cations and anions that compose the ore minerals. Thus, deposition of gangue minerals can deplete the hydrothermal fluid in ions that are required to form ores and consequently, even if all

other factors, including the concentration of the metal in the fluid, are favorable, a deposit may not form. Deposition of gangue minerals also may lead to the dissolution of an ore mineral, if the gangue minerals have ions in common with the ore mineral, leading to an increase in the metal concentration of the fluid and deposition of ore in larger amounts at some other location. Understanding the role of gangue minerals in controlling the solubility of ore minerals, therefore, is an important step in developing predictive tools for the exploration of metallic mineral deposits.

Tungsten is a critical metal used widely in aerospace and other high-technology industries. This metal is supplied mainly by deposits that are genetically associated with highly fractionated S-type granites characterized by relatively high contents of P_2O_5 (0.11–0.40 wt%) and F (0.19–0.99 wt%) (Polya, 1989; Lu et al., 2003; Wu et al., 2017). Moreover, apatite and fluorite are very common gangue minerals in these deposits (Polya, 1989; Soloviev and Kryazhev, 2017; Song et al., 2018a, 2018c; Xie et al., 2019; Roy-Garand et al., 2022). This indicates that the ore-forming fluids are relatively enriched in phosphorus and fluorine. Apatite and fluorite are also

abundant in some albites, which are considered to record the pathways of the ore-forming fluids (Rasmussen et al., 2011; Song et al., 2020). In addition, it is noteworthy that the remobilization of tungsten from scheelite- and/or wolframite-bearing rocks, including *endo*-skarns, greisens, and albites, and accompanying fluorite and/or apatite deposition is a very common feature of many tungsten deposits (e.g., Tikus Sn-W, Schwartz and Surjono, 1990; Mount Pleasant W-Mo-Sn, Samson, 1990; Shizhuyuan W-Sn-Mo-Bi, Jingwen et al., 1996; Lu et al., 2003; Kyzyltau W, Graupner et al., 1999; Carris W-Mo-Sn, Moura et al., 2014; Dahutang W, Huang and Jiang, 2014; Song et al., 2018c; Huangshaping W, Ding et al., 2018; Weodong W, Choi et al., 2020; Cuonadong Be-W-Sn, Xie et al., 2020; Huangtian W, Han et al., 2020; Sandaozhuang W, Zhan et al., 2021). Indeed, at Zhuxi (one of the largest tungsten deposits in the World, with resource of 3.44 Mt WO_3), the replacement of early disseminated scheelite in the associated granitic intrusions, albitites, and *endo*-skarns by fluorite and/or apatite is interpreted to have supplied much of the tungsten for the main stage, vein-controlled scheelite mineralization (Song et al., 2018a, 2018b, 2020). Thus, a question that is deserving of consideration is whether phosphorus and fluorine play a direct role in tungsten ore genesis or are just bystanders to the process.

Numerous studies have proposed that tungsten ore minerals (scheelite and wolframite) deposit in response to cooling, fluid-mixing or fluid-rock interaction from low salinity, aqueous-carbonic fluids at temperatures between 250 and 350 °C (Campbell and Robinsoncook, 1987; Polya, 1989; Wood and Samson, 2000; Bailly et al., 2002; Wei et al., 2012; Ni et al., 2015; Lecumberri-Sanchez et al., 2017; Legros et al., 2019; Pan et al., 2019; Yang et al., 2019; Ni et al., 2022), and a number of studies have proposed that the tungsten in these fluids is transported primarily as the species, H_2WO_4, HWO_4^-, and WO_4^{2-} (Wesolowski et al., 1984; Wood and Samson, 2000; Wang et al., 2019; Wang et al., 2020; Carocci et al., 2022; Qiu et al., 2022), or $H_3WO_4F_2^-$, if the fluids are fluorine-bearing (Wang et al., 2021). In evaluating tungsten transport and deposition, however, few researchers have given consideration to the role of apatite and fluorite in buffering calcium and fluorine ion activity, thereby controlling scheelite solubility, or the role of phosphate as a transport ligand for tungsten that could also affect scheelite solubility; phosphate is a hard ligand that is likely to form strong complexes with tungsten (Pearson, 1963; Williams-Jones and Migdisov, 2014).

In order to better understand the factors controlling the hydrothermal transport and deposition of tungsten, we carried out experiments designed to evaluate the solubility of scheelite at 250 and 350 °C in P- and/or F-bearing aqueous solutions with pH values from 2 to 7, i.e., from acidic to slightly alkaline. The results clearly show that the phosphate and fluoride ions combine with calcium released from scheelite to form apatite and fluorite, thereby sharply increasing the solubility of tungsten, especially in fluids with near neutral to neutral pH. They also show that both fluoride and phosphate can act as transport ligands for tungsten. This research was complemented by the modeling of tungsten transport and deposition, the results of which indicate that magmatic-hydrothermal phosphorus- and fluorine-rich fluids can be greatly enriched in tungsten during the alteration of granites to *endo*-greisens and albitites, leading to the formation of high-grade tungsten ores. The observations of the competition between ore and gangue minerals may also apply to other types of hydrothermal ore deposits.

2. Methods

2.1. Solubility experiments

The experimental equipment and methods adopted in this study are the same as those used in previous studies at McGill University (Migdisov and Williams-Jones, 2007; Wang et al., 2021). The fluorine-free experiments were carried out in batch-type titanium grade 2 autoclaves (Fig. S1a), and the fluorine-bearing experiments in Teflon test tubes contained in stainless steel autoclaves (Fig. S1b). In both sets of experiments, the autoclaves were heated in an oven. Scheelite solubility ($CaWO_4$) was investigated in 0.5 m NaCl aqueous solutions of variable fluorine and phosphorus concentration and pH at temperatures of 250 and 350 °C, and vapor-saturated water pressure. The fluorine-bearing solutions were prepared by adding NaF solid to nano-pure water in amounts that yielded fluoride concentrations ranging from 0.005 mol/kg to 0.25 mol/kg; the pH of the solutions was controlled by adding HCl, and varied from 2 to 7 at the temperature of the experiments. The phosphorus-bearing solutions were prepared by adding NaH_2PO_4 and Na_2HPO_4 solid to nano-pure water in amounts that yielded phosphorus concentrations ranging from 0.005 mol/kg to 0.02 mol/kg; the pH of the solutions was controlled by adding HCl and varied from 3 to 7 at the temperature of the experiments. Finally, the fluorine- and phosphorus-bearing solutions were prepared by adding NaF and NaH_2PO_4 solid to nano-pure water in amounts that yielded fluorine concentrations varying from 0.005 mol/kg to 0.05 mol/kg and phosphorus concentrations ranging from 0.005 mol/kg to 0.02 mol/kg. The pH of the solutions was controlled by adding HCl and varied from 3 to 7 at the experimental temperature; the amount of HCl that needed to be added to the solutions was calculated using HCh software (Shvarov, 2008).

The solid reactant, scheelite ($CaWO_4$), used in the experiments was extracted from a rock collected from the Yaogangxian deposit, China. The scheelite crystals were crushed and the grains (20–60 mesh) were hand-picked under a binocular microscope equipped with ultraviolet light. The purity of the grains is >99%; the <1% impurity is due to microscopic inclusions of ankerite ($Ca_{0.5}(Fe, Mg)_{0.5}CO_3$) and fluorite. Representative scheelite grains were analyzed by EPMA, results of which are listed in Table S1. After separation, the scheelite grains were cleaned in an ultrasonic bath, dried and introduced into a small Teflon holder and titanium holder (∼3 cm long) for fluorine-bearing and -free experiments, respectively. The holders were then capped by Teflon wool and titanium fragments, respectively, to prevent mechanical transfer of the solid to the solution. At the beginning of each experiment, 16 ml of experimental solution was added to the Teflon reactor (fluorine-bearing) or titanium autoclave (fluorine-free).

The experiments were conducted for durations of 12–19 days, which greatly exceeded the time taken in previous experimental studies of tungsten trioxide solubility in fluorine-bearing and -free experiments for tungsten to reach a steady state concentration at temperatures of 100 and 250 °C (6–7 days) (Wang et al., 2019; Wang et al., 2021). This ensured that tungsten reached a steady state concentration in the experiments described here. At the end of each set of experiments, the autoclaves were removed from the oven and quenched in water to ambient temperature in <20 min. A 4 ml aliquot of solution was taken from each tube for pH determination and analysis of the fluoride concentration. Four ml of 0.65 m NaF solution and four ml of 1 m NaOH solution was then added to each tube in the fluorine-bearing and fluorine-free experiments, respectively, to dissolve any tungsten that had precipitated on the walls of the reactor during quenching. After 30 min, the mixed solution was removed for analysis of its tungsten content. The pH and fluoride concentration were measured using an InLab™ Hydrofluoric Electrode and Thermo Scientific™ Orion™ Fluoride Electrode purchased from Fisher Scientific. Solutions containing >0.1 mol/kg Na^+ and 0.01 mol/kg HF were diluted with distilled water prior to measuring their pH. Tungsten concentrations were analyzed using Inductively Coupled Plasma Mass Spectrometry after 2,000–250,000 times dilution of the experi-

mental solution using a 0.005 wt% NaF solution. The analyses were conducted at the State Key Laboratory of Ore Deposit Geochemistry, Institute of Geochemistry, Chinese Academy of Sciences. The compositions of the initial and quenched experimental solutions are listed in Table 1.

2.2. SEM and EPMA analyses of reaction products

After each experiment, the reaction products were washed in nano-pure water and dried at 60 °C for two days and then removed for scanning electron microscope (SEM) analyses. Backscattered electron images of the solid reaction products were created using a JSM-7800F scanning electron microscope. The solid reaction products were then mounted in epoxy resin and polished for EPMA. Contents of the major and minor elements in apatite were determined using a JOEL-1600 electron microprobe with a 25 kV accelerating voltage, a 10 nA beam current, and a 3–10 μm beam diameter. The following minerals were used for apatite composition calibration: pyrope garnet (Al, Mg, Fe, Mn), albite (Na), apatite (Ca, P, F, Sr), and tugtupite (Cl). Detection limits were 0.07 wt% for F, 0.03 wt% for Na, 0.04 wt% for Sr, 0.02 wt% for Al, Mg, and P, 0.01 wt% for Ca, Cl, Fe, and Mn. The SEM and EPMA analyses were all carried out at the State Key Laboratory of Ore Deposit Geochemistry, Institute of Geochemistry, Chinese Academy of Sciences. Results of the electron probe microanalyses of representative apatite and scheelite crystals from the experiments are reported in Table S2. The formulae for end-member F-, Cl- and OH-Apatite were calculated as follows (Piccoli and Candela, 2002): Fap, the mole fraction of fluorapatite in apatite, was determined using the relationship $X_{FAp}^{Ap} = C_F^{Ap}/3.767$, where C_F^{Ap} is the concentration of F in apatite in wt.%; CAp is the mole fraction of chlorapatite ($X_{ClAp}^{Ap} = C_{Cl}^{Ap}/6.809$) and HAp is the mole fraction of hydroxylapatite ($X_{HAp}^{Ap} = 1 - X_{FAp}^{Ap} - X_{ClAp}^{Ap}$).

2.3. Scheelite solubility calculation

The solubility of scheelite in the fluorine-bearing solutions was calculated using the HCh software package (Shvarov, 2008), assuming that tungsten dissolved as the species $H_2WO_4^0$, HWO_4^-, WO_4^{2-}, and $H_3WO_4F_2^-$. In addition to these tungsten species, the following aqueous species, O_2, H_2, H^+, OH^-, Na^+, Cl^-, F^-, $NaOH^0$, $NaCl^0$, NaF^0, HCl^0, HF^0, Ca^{2+}, $CaCl^+$, $CaCl_2^0$, $Ca(OH)^+$, CaF^+, and the solid phases, scheelite and fluorite were considered in the calculations. The sources of these data and the data for the other aqueous species and minerals (Kiseleva et al., 1980; Williams-Jones and Seward, 1989; Robie and Hemingway, 1995; Shock et al., 1997; Sverjensky et al., 1997; Tagirov et al., 1997; Wood and Samson, 2000; Pokrovski et al., 2002; Holland and Powell, 2011; Zimmer et al., 2016; Wang et al., 2019; Wang et al., 2021) are listed in Table S3. The activity coefficient of each ionic species at the different experimental conditions was calculated using the extended Debye-Hückel equation (Helgeson et al., 1981; Oelkers and Helgeson, 1990, 1991):

$$\log \gamma_n = -\frac{A \cdot [z_n]^2 \cdot \sqrt{I}}{1 + B \cdot \mathring{a} \cdot \sqrt{I}} + b_\gamma \cdot I + \Gamma \qquad (1)$$

in which A and B are constants representing Debye-Hückel limiting law parameters, b_γ is the extended parameter for NaCl from Helgeson and Kirkham (1974), $\mathring{a}$ is the distance of closest approach, which is specific to the ion of interest, z is the charge of the ion, Γ is a molarity to molality conversion factor, and I is the ionic strength calculated using Eq. (2):
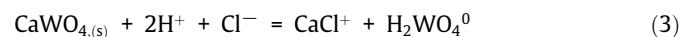
$$I = \frac{1}{2} \sum_{i=1}^{n} c_i z_i^2 \qquad (2)$$

where c_i is the molar concentration of ion i (mol/kg) and z_i is the charge of that ion. Parameter I represents the true ionic strength as all the dissolved components that were considered. The activity coefficients of the neutral species were assumed to be unity. The Haar-Gallagher-Kell and Marshall and Franck models were used to determine the thermodynamic properties and disassociation constant of H_2O, respectively, for our experimental conditions (Marshall and Franck, 1981; Kestin et al., 1984).

3. Results

3.1. Fluorine- and phosphorous-free solutions

In order to determine the solubility of scheelite in fluorine- and phosphorus-free aqueous solutions, experiments were carried out at 250 °C in aqueous solutions containing 0.5 m NaCl (~2.5 wt%) with pH_T values in the range 3.5–6.5. The pH_T represents the calculated pH of the starting experimental solutions at the temperature of interest. At these conditions, the concentration of tungsten was low, in the range 1.01–9.82 ppm (Table 1). Experiments were also carried out at 350 °C using the same solution for a pH_T of 6. For these conditions, the concentration of dissolved tungsten was 11.9 ppm. Finally, a set of experiments was conducted at 250 °C for a pH_T of 6, in which the NaCl concentration was varied from 0.5 m to 1.5 m NaCl. The tungsten concentration increased with increasing NaCl concentration from 7.31 to 11.5 ppm. Examination of the scheelite with a SEM after the experiments showed that it was unchanged from the unreacted scheelite. The very limited dissolution of scheelite was mainly via Reactions (3)–(5):

$$CaWO_{4,(s)} + 2H^+ + Cl^- = CaCl^+ + H_2WO_4^0 \qquad (3)$$

$$H_2WO_4^0 = H^+ + HWO_4^- \qquad (4)$$

$$HWO_4^- = H^+ + WO_4^{2-} \qquad (5)$$

3.2. Fluorine-bearing solutions

Experiments investigating the solubility of scheelite in fluorine-bearing solutions were carried out at 250 °C and comprised three series. In the first series, the fluorine concentration was held constant at a high value (0.15 m NaF) and in the second series it was held constant at a low value (0.01 m NaF). The pH_T in both series was varied between 2 and 6.75. The third series was conducted at a constant pH_T of 6 in solutions with NaF concentrations varying between 0 and 0.25 m NaF.

In the experiments with solutions containing a constant NaF molality of 0.15, the concentration of dissolved tungsten increased from 10.1 ppm to 3,433 ppm as pH_T increased from 2 to 6.75 (Fig. 1a). By contrast, in solutions containing 0.01 m NaF (190 ppm $\sum$F), the concentration of dissolved tungsten increased from 15.4 to 54.9 ppm as the pH_T increased from 3.5 to 6.5 (Fig. 1b). The relative importance of hydrogen ion activity and fluorine concentration on the solubility of scheelite was evaluated with the third series of experiments (at a pH_T of 6 and mNaF between 0 and 0.25 m). The concentration of dissolved tungsten increased from 4 ppm in the fluorine-free fluid to 313 ppm in a fluid containing 0.03 m NaF (515 ppm F) and 3140 ppm in the fluid containing 0.25 m NaF (Fig. 1c).

Back scattered scanning electron microscope (BSE) images of the solid reaction products from the first series of experiments, show that at pH values <5, the scheelite reacted with fluoride to produce fluorite and WO_3 crystals. However, they also show that the mass of WO_3 decreased with increasing pH and the shape of the WO_3 crystals changed from plate-like (Fig. 2a) to needle-like

Table 1

Compositions of the experimental solutions. The content of NaF, NaCl, HCl, NaOH, NaH_2PO_4 and Na_2HPO_4 represent the starting composition. The pH_T value was calculated from the starting compositions at the experimental temperature. The contents of tungsten (mW), fluorine (mF), and the pH were measured in the quenched experimental solutions at 25 °C; the concentration of W is in ppm.

Run No.	pH_T	mNaF	mNaCl	mHCl	mNaOH	$mNaH_2PO_4$	mNa_2HPO_4	pH quench	mF quench	mW (ppm)
250 °C										
12–3	3.5	0	0.5	0.000839	0	0	0	4.062	0.001	4.11
12–4	4	0	0.5	0.000265	0	0	0	3.38	0.0073	9.82
12–5	4.5	0	0.5	0.0000833	0	0	0	3.661	0.0035	5.93
12–6	5	0	0.5	0.0000249	0	0	0	4.233	0.0008	5.56
12–7	5.5	0	0.5	0	0	0	0	4.7	0.0003	5.01
12–8	6	0	0.5	0	0.000014	0	0	4.447	0.0006	7.31
12–9	6.5	0	0.5	0	0.000052	0	0	4.895	0.0006	1.01
12–21	5.6	0	0.5	0	0	0	0	3.988	0.0013	3.88
8–2	5.6	0	1	0	0	0	0	4.488	0.0007	6.19
12–22	5.6	0	1	0	0	0	0	4.720	0.0007	8.93
8–3	5.6	0	1.5	0	0	0	0	4.764*	0.0006	9.51
12–23	5.6	0	1.5	0	0	0	0	3.429	0.006	11.5
5–1	2	0.15	0.5	0.179	0	0	0	2.788*	0.051	10.1
5–2	2.2	0.15	0.5	0.168	0	0	0	2.770*	0.066	18.9
5–3	2.4	0.15	0.5	0.161	0	0	0	2.814*	0.048	27.5
5–4	2.8	0.15	0.5	0.154	0	0	0	2.834*	0.057	37.9
5–5	3	0.15	0.5	0.151	0	0	0	2.868*	0.054	39.3
5–6	3.2	0.15	0.5	0.150	0	0	0	2.910*	0.057	50.0
5–7	3.4	0.15	0.5	0.148	0	0	0	2.860*	0.067	100
5–8	3.6	0.15	0.5	0.145	0	0	0	2.868*	0.069	112
5–9	3.8	0.15	0.5	0.142	0	0	0	2.866*	0.079	160
5–10	4	0.15	0.5	0.137	0	0	0	2.902*	0.080	257
5–11	4.5	0.15	0.5	0.114	0	0	0	3.056*	0.085	566
5–12	4.75	0.15	0.5	0.0965	0	0	0	3.200*	0.096	905
5–13	5	0.15	0.5	0.0754	0	0	0	3.421*	0.106	1296
5–14	5.25	0.15	0.5	0.0544	0	0	0	3.743*	0.110	1465
5–15	5.5	0.15	0.5	0.0363	0	0	0	4.343*	0.109	1753
5.16	5.75	0.15	0.5	0.0228	0	0	0	6.212*	0.110	2961
5–17	6	0.15	0.5	0.0138	0	0	0	6.153*	0.110	2579
5–18	6.25	0.15	0.5	0.00802	0	0	0	6.442*	0.108	2831
5–19	6.5	0.15	0.5	0.00459	0	0	0	6.539*	0.112	3353
5–20	6.75	0.15	0.5	0.00255	0	0	0	6.533*	0.111	3433
12–12	3.5	0.01	0.5	0.0106	0	0	0	3.28	0.0096	15.4
12–14	4.5	0.01	0.5	0.00782	0	0	0	3.442	0.0091	27.3
10–13	5	0.01	0.5	0.00522	0	0	0	3.719	0.010	26.5
12–15	5	0.01	0.5	0.00522	0	0	0	3.809	0.0087	32.2
12–16	5.5	0.01	0.5	0.00255	0	0	0	4.067	0.0091	40.4
12–17	6	0.01	0.5	0.000962	0	0	0	4.913	0.0089	54.9
12–18	6.5	0.01	0.5	0.000279	0	0	0	4.46	0.0104	52.5
7–1	6	0	0.5	0.0000138	0	0	0	3.928	0.0002	4.15
7–5	6	0.005	0.5	0.000474	0	0	0	4.694	0.0046	19.1
7–7	6	0.01	0.5	0.000962	0	0	0	4.139	0.0106	68.9
10–14	6	0.01	0.5	0.000962	0	0	0	4.250	0.010	37.9
12–39	6	0.01	0.5	0.000962	0	0	0	4.481	0.0104	38.7
7–8	6	0.02	0.5	0.00193	0	0	0	4.735	0.0186	188
12–40	6	0.02	0.5	0.00193	0	0	0	5.053	0.0188	179
7–9	6	0.03	0.5	0.00290	0	0	0	5.160	0.0271	305
7–10	6	0.04	0.5	0.00385	0	0	0	5.414	0.0349	457
12–42	6	0.04	0.5	0.00385	0	0	0	5.317	0.0368	579
7–11	6	0.05	0.5	0.00481	0	0	0	6.182	0.0408	657
12–43	6	0.05	0.5	0.00481	0	0	0	6.074	0.0388	672
7–12	6	0.06	0.5	0.00575	0	0	0	5.613	0.0497	710
7–13	6	0.08	0.5	0.00763	0	0	0	5.849	0.0614	1028
7–14	6	0.1	0.5	0.00950	0	0	0	5.440*	0.0657	1099
7–15	6	0.125	0.5	0.0118	0	0	0	5.756*	0.0766	1429
7–16	6	0.15	0.5	0.0141	0	0	0	6.271*	0.1070	2370
7–17	6	0.175	0.5	0.0164	0	0	0	5.605*	0.100	2168
7–18	6	0.2	0.5	0.0186	0	0	0	5.313*	0.090	1852
7–19	6	0.225	0.5	0.0208	0	0	0	5.426*	0.122	2525
7–20	6	0.25	0.5	0.0230	0	0	0	5.581*	0.144	3140
13–3	3.5	0	0.5	0.00518	0	0.01	0	3.632	0	16.4
13–4	3.8	0	0.5	0.00519	0	0.008	0.002	3.804	0	28.3
13–5	4	0	0.5	0.00521	0	0.007	0.003	4.023	0	30.1
13–6	4.5	0	0.5	0.00522	0	0.00556	0.00444	4.667	0	30.0
13–7	5	0	0.5	0.00522	0	0.005	0.005	5.133	0	45.0
13–8	5.5	0	0.5	0.00520	0	0.00474	0.00526	5.186	0	48.8
13–9	6	0	0.5	0.00408	0	0.0055	0.0045	5.636	0	92.9
13–10	6.5	0	0.5	0.00322	0	0.0055	0.0045	5.964	0	121
13–11	6	0	0.5	0.00229	0	0.0025	0.0025	5.395	0	39.6
13–12	6	0	0.5	0.00688	0	0.0075	0.0075	5.655	0	107
13–13	6	0	0.5	0.00917	0	0.01	0.01	5.662	0	138

Table 1 (*continued*)

Run No.	pH_T	mNaF	mNaCl	mHCl	mNaOH	$mNaH_2PO_4$	mNa_2HPO_4	pH quench	mF quench	mW (ppm)
8–21	3.5	0.01	0.5	0.0149	0	0.01	0	3.217	0.0108	91.5
12–28	3.5	0.01	0.5	0.0149	0	0.01	0	3.016	0.0163	75.1
13–22	3.5	0.01	0.5	0.0149	0	0.01	0	3.234	0.0129	40.9
8–22	4	0.01	0.5	0.0114	0	0.01	0	3.363	0.0118	99.5
13–23	4	0.01	0.5	0.0114	0	0.01	0	3.378	0.0142	58.0
13–24	4.5	0.01	0.5	0.00850	0	0.01	0	3.516	0.0124	95.6
8–24	5	0.01	0.5	0.00539	0	0.01	0	3.709	0.0112	105
8–25	5.5	0.01	0.5	0.00247	0	0.01	0	4.047	0.0096	133
8–26	6	0.01	0.5	0.000550	0	0.01	0	4.766	0.0109	184
8–27	6.5	0.01	0.5	0	0.000960	0.01	0	5.782	0.0099	227
8–28	6	0.01	0.5	0.000758	0	0.005	0	4.511	0.0103	125
8–29	6	0.01	0.5	0.000550	0	0.01	0	4.658	0.011	196
8–30	6	0.01	0.5	0.000340	0	0.015	0	4.878	0.0112	228
8–31	6	0.01	0.5	0.000126	0	0.02	0	5.022	0.0098	247
12–37	6	0.01	0.5	0.000126	0	0.020	0	4.913	0.0108	248
8–39	6	0.03	0.5	0.00268	0	0.005	0	4.699	0.0252	292
10–16	6	0.03	0.5	0.00246	0	0.01	0	4.881	0.0361	355
8–41	6	0.03	0.5	0.00224	0	0.015	0	4.721	0.0265	374
8–42	6	0.03	0.5	0.00202	0	0.02	0	4.784	0.0273	430
8–33	6	0.005	0.5	0.0000690	0	0.01	0	4.888	0.0048	111
8–34	6	0.01	0.5	0.000550	0	0.01	0	4.778	0.0111	217
8–35	6	0.02	0.5	0.00151	0	0.01	0	4.451	0.0198	223
10–15	6	0.02	0.5	0.00151	0	0.01	0	4.256	0.0219	169
12–44	6	0.02	0.5	0.00151	0	0.01	0	4.547	0.0213	193
12–45	6	0.03	0.5	0.00246	0	0.01	0	5.067	0.0277	351
12–20	6	0.04	0.5	0.00341	0	0.01	0	6.093	0.0333	604
12–46	6	0.04	0.5	0.00341	0	0.01	0	6.000	0.0347	456
8–38	6	0.05	0.5	0.00436	0	0.01	0	5.961	0.0405	676
12–48	6	0.05	0.5	0.00436	0	0.01	0	6.336	0.0416	711
350 °C										
9–13	3.33	0	0.5	0.0173	0	0.01	0	3.059	0	41.6
9–14	4	0	0.5	0.0151	0	0.005	0.005	3.448	0	32.9
11–4	4.00		0.5	0.0151	0	0.005	0.005	3.404	0	48.5
9–15	4.5	0	0.5	0.0118	0	0.005	0.005	3.398	0	28.3
11–5	4.50	0	0.5	0.0118	0	0.005	0.005	3.547	0	52.6
9–16	5.09	0	0.5	0.00519	0	0.008	0.002	3.743	0	47.4
9–17	5.30	0	0.5	0.00521	0	0.007	0.003	3.979	0	89.1
9–20	6.64	0	0.5	0.00520	0	0.00474	0.00526	5.33	0	138
11–1	6	0	0.5	0.0000111	0	0	0	4.644	0.0005	15.1
11–2	6	0	0.5	0.0000111	0	0	0	5.581	0.0002	8.70
9–21	6	0	0.5	0.00275	0	0.0025	0.0025	5.386	0	81.0
9–22	6	0	0.5	0.00548	0	0.005	0.005	5.123	0	124
9–23	6	0	0.5	0.00821	0	0.0075	0.0075	5.334	0	225
9–24	6	0	0.5	0.0109	0	0.01	0.01	5.377	0	268

Note: *These pH (quench) values represent the pH value of the quenched solutions after 20 times dilution. The other pH (quench) values listed in the table represent the pH value of the quenched solutions after 10 times dilution.
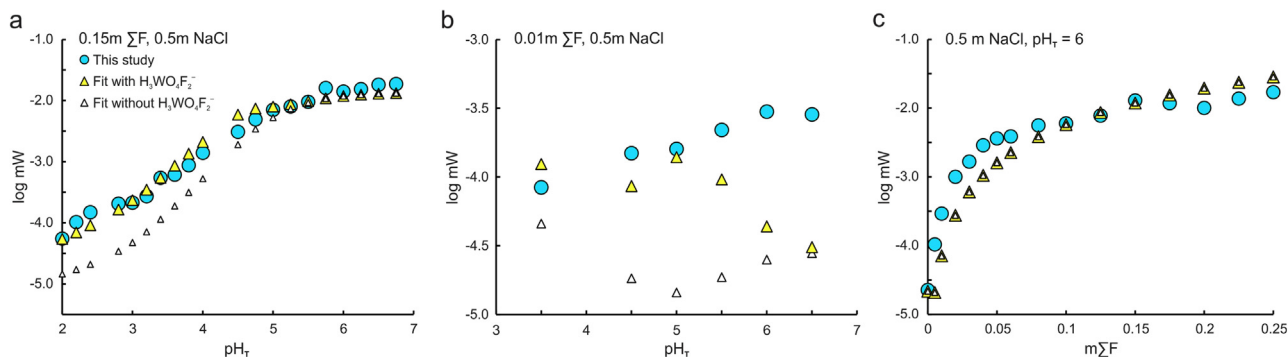
Fig. 1. Results of scheelite solubility experiments in fluorine-bearing aqueous solutions at 250 °C. They show the concentration of dissolved tungsten (log mΣW) (a) as a function of pH_T in solutions containing 0.15 m NaF and 0.5 m NaCl, (b) as a function of pH_T in solutions containing 0.01 m NaF and 0.5 m NaCl, and (c) as a function of the molality of fluorine in a 0.5 m NaCl solution at a pH_T of 6. The filled blue circles illustrate the results of the experiments. The filled blue circles represent the concentrations of tungsten determined experimentally; the filled white triangles represent tungsten concentrations calculated from thermodynamic data for the tungstate species, $H_2WO_4^0$, HWO_4^-, and WO_4^{2-}, and the filled yellow triangles for these species plus those for $H_3WO_4F_2^-$. (For interpretation of the references to colour in this figure legend, the reader is referred to the web version of this article.)
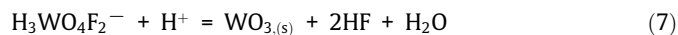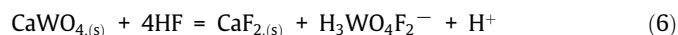
(Fig. 2b; Fig. S2). The WO$_3$ solid ceased to precipitate at a pH$_T$ of 5 (Fig. 2c). In reactions involving solutions (0.15 m NaF) having a pH$_T$ of 5–6.75, only fluorite formed (Fig. 2c–e). Furthermore, the nature of the fluorite changed from large amorphous masses that replaced scheelite (the source of the calcium) to small octahedra that crystallised on the surface of the scheelite and in cavities on this surface (Fig. 2d and e). This indicates that replacement of scheelite by fluorite gave way to saturation of the fluid with fluorite and that the rate of growth of fluorite gradually exceeded its rate of nucleation with increasing pH$_T$.

In order to better understand the dissolution process, we calculated the solubility of scheelite in the solutions and used these data to fit the experimental data. Two sets of calculations were performed. The first set employed thermodynamic data for H$_2$WO$_4$, HWO$_4^-$, WO$_4^{2-}$ and H$_3$WO$_4$F$_2^-$ (Shock et al., 1997; Wang et al., 2019; Wang et al., 2021), and the second did not consider H$_3$WO$_4$F$_2^-$. The results of the calculations are illustrated in Fig. 1a for the high mNaF (0.15 m) series and show that up to a pH of 5, the best fit to the experimental data (a nearly perfect fit) is obtained using the first set of calculated solubility data. At higher pH, the two sets of solubility data are almost indistinguishable and essentially the same as the experimentally determined solubility data (Fig. 1a). This indicates that at a pH < 5, the solubility of scheelite is increased considerably by the formation of H$_3$WO$_4$F$_2^-$ but that at higher pH it is satisfactorily accommodated by fluorine-free tungstate species.

As discussed above, the dissolution of scheelite in fluorine-bearing solutions (0.15 m NaF) was accompanied by the formation of abundant fluorite (Fig. 2), which, as illustrated by Reaction (6), caused the release of a large amount of tungsten to the solution. At low pH, however, this release of tungsten, mainly as H$_3$WO$_4$F$_2^-$, exceeded the amount of tungsten that could be dissolved and, consequently, the solution saturated with WO$_3$ solid (Fig. 2a and b; Reaction (7)); initially, the solution was strongly oversaturated with respect to the WO$_3$ solid, but the degree of oversaturation decreased with increasing pH and at a pH > 5, the solution was undersaturated with respect to this phase. At higher pH, the greater stability of the dissolved tungsten species, dominantly WO$_4^{2-}$, prevented the precipitation of WO$_3$ solid, and the low solubility of fluorite and decreasing hydrogen ion activity ensured that scheelite dissolution and the molality of dissolved tungsten continued to climb (Fig. 1; Reaction (8)); the increased dissociation of HF with increasing pH contributed to the precipitation of fluorite (and H$_3$WO$_4$F$_2^-$ stability) by increasing the availability of F$^-$ ions.

$$CaWO_{4,(s)} + 4HF = CaF_{2,(s)} + H_3WO_4F_2^- + H^+ \qquad (6)$$

$$H_3WO_4F_2^- + H^+ = WO_{3,(s)} + 2HF + H_2O \qquad (7)$$

$$CaWO_{4,(s)} + 2F^- = CaF_{2,(s)} + WO_4^{2-} \qquad (8)$$

It may be recalled that for the experiments conducted at a low concentration of NaF (0.005–0.06 m) and a pH > 5, the concentrations of tungsten determined experimentally were significantly higher than those calculated from the thermodynamic data for the two sets of tungsten species referred to above (Fig. 1b and c). This is due to the fact that in fitting the results, the calculated amount of fluorite was zero or much less than detected in the SEM analyses. For example, in the solution containing 0.005 m NaF at a pH$_T$ of 6, a small proportion of fluorite was detected (Fig. 2f), but no fluorite was calculated to form using the thermodynamic data currently available for fluorite.

3.3. Phosphorous-bearing solutions

Experiments involving phosphorous were carried out at 250 and 350 °C in two series. In the first series, the phosphorous concentration was held constant at a low value (0.01 m, 310 ppm $\sum$P) as the pH$_T$ was increased from 3 to 6.5 or 7. The second series was conducted at a constant pH of 6 for solutions with phosphorous concentrations varying between 0.005 and 0.02 m.
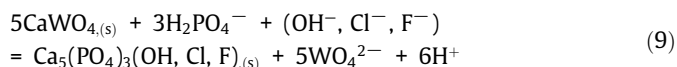
In the first series of experiments conducted with solutions containing a constant $\sum$P concentration of 0.01 m at 250 °C, the con-
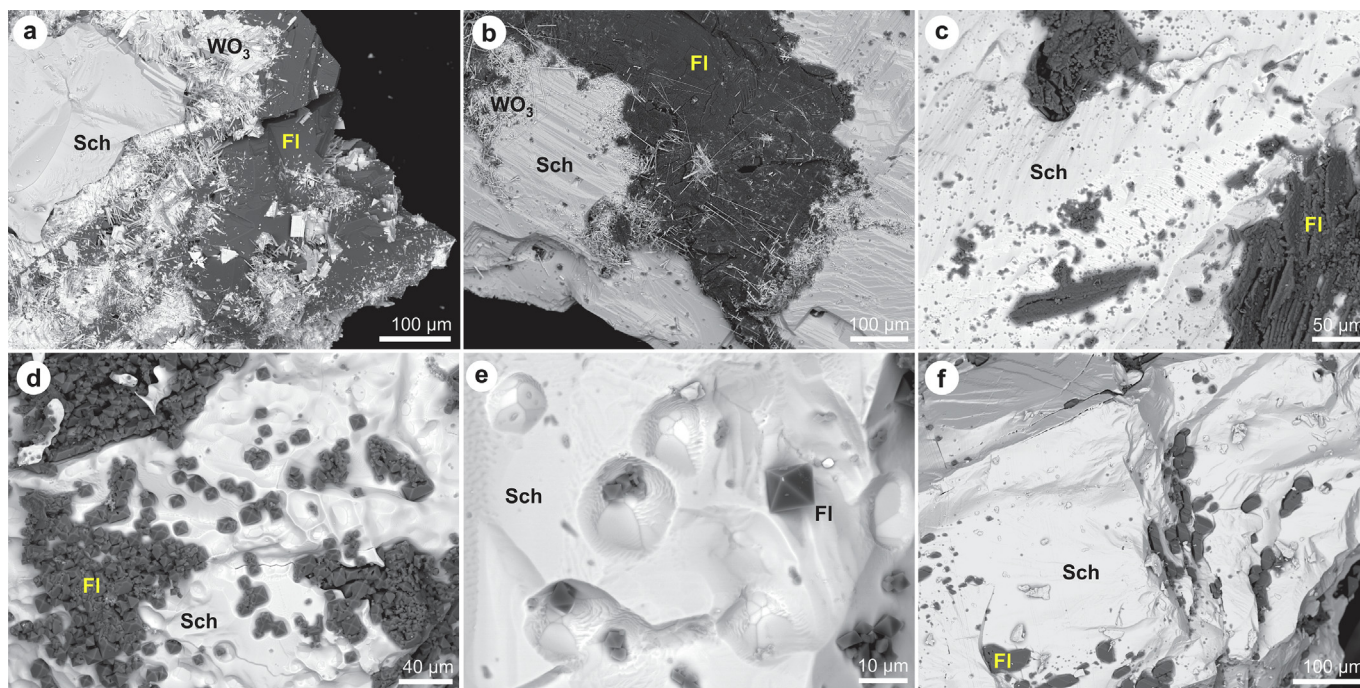
Fig. 2. Backscattered electron (BSE) images of the solid run products of the scheelite dissolution experiments. These experiments involved solutions containing 0.15 m NaF and 0.5 m NaCl, (a) at a pH$_T$ of 2; (b) at a pH$_T$ of 4.5 (an enlargement of this image is provided in Fig. S2); (c) at a pH$_T$ of 5; (d) and (e) at a pH$_T$ of 6.75. (f) A BSE image of the scheelite after reaction with a solution containing 0.005 m NaF and 0.5 m NaCl at a pH$_T$ of 6.

centration of tungsten increased from 16.4 to 121 ppm as pH_T increased from 3.5 to 6.5 (Fig. 1a), whereas in the second series at the same temperature, a constant pH_T of ~6 and $m\sum P$ varying from 0.005 m to 0.2 m, the concentration of tungsten increased from 39.6 ppm to 138 ppm (Fig. 3b). The experiments conducted at 350 °C and variable pH_T yielded results very similar to those obtained for 250 °C, i.e., for solutions containing 0.01 $m\sum P$, the concentration of dissolved tungsten increased from 32.9 to 138 ppm as the pH_T increased from 3 to 7 (Fig. 3a). In contrast, at a constant pH_T of 6, the concentration of dissolved tungsten increased from 8.7 ppm to 268 ppm in a fluid containing 0.02 $m\sum P$ (Fig. 3b).

Back scattered electron images of the solids from the experiments at 250 and 350 °C show that no apatite formed at a pH < 4. In the experiments conducted with solutions having a pH_T of 4–6.5, only apatite formed (Fig. 4a–c; Fig. S3). The BSE images show that apatite formed, even at a phosphorus concentration of 0.005 m (Fig. 4b). The amount, nature, and composition of the apatite crystallizing in the phosphate-bearing solutions varied with the pH_T of the solution. At pH_T values of 4–5.5, the apatite abundance was relatively low, the crystals were equidimensional, and the composition was that of hydroxyapatite with a relatively high chloride concentration, whereas at pH_T values of 5.5–6.5, apatite was much more abundant, the crystals were prismatic and the composition was that of hydroxyapatite with a low chlorine content (Fig. 4; Table S2). The chlorine content correlates negatively with pH_T (Fig. S4). The dissolution of scheelite in these experiments can be described by Reaction (9).

$$5CaWO_{4,(s)} + 3H_2PO_4^- + (OH^-, Cl^-, F^-) = Ca_5(PO_4)_3(OH, Cl, F)_{,(s)} + 5WO_4^{2-} + 6H^+ \quad (9)$$

3.4. Phosphorous-fluorine-bearing solutions

All the experiments involving solutions containing both fluorine and phosphorus were conducted at 250 °C and comprised three series. The first series was conducted at a constant phosphorous and fluorine concentration (0.01 m $\sum P$ and 0.01 m $\sum F$) with pH_T varying from 3.5 to 6.5. In the second series, the fluorine concentration was low (0.01 m $\sum F$) and in the third series was slightly higher (0.03 m NaF). The latter two series were conducted at a constant pH of 6 and for phosphorous concentrations that varied between 0 and 0.02 m.

From Fig. 3a, it is evident that, for solutions containing 0.01 m $\sum P$ and 0.01 m $\sum F$, the concentration of dissolved tungsten increased from ~69 to 227 ppm as the pH_T increased from 3.5 to 6.5. In the experiments with solutions containing 0.01 m F at a constant pH_T of 6, the tungsten concentration increased from 125 ppm to 284 ppm as the phosphorous concentration increased from 0.005 m to 0.02 m (Fig. 3b), and in experiments containing 0.03 m F for the same range of phosphorus concentration, the concentration of tungsten increased from 292 ppm to 430 ppm (Fig. 3b).

Backscattered electron images of the solid products of these experiments show that scheelite reacted with phosphate and fluorine and generated fluorite and fluorapatite (Fig. 4e–i). The proportions of fluorite and fluorapatite varied depending on the contents of phosphate and fluorine. Fluorapatite dominated and was accompanied by minor fluorite in experiments for which the fluorine to phosphate mole ratio in the solution was <2 (Fig. 4e–g; Fig. S5a and S5b), whereas fluorapatite and fluorite were the major phases, if this ratio was between 2 and 5 (Fig. 5h; Fig. S5c), and fluorite was dominant if the ratio was >5 (Fig. 5i; Fig. S5d). Significantly, the solubility of scheelite in the 0.01 m P solutions with F concentrations < 0.02 (mF/mP < 2) was higher than in the fluorine-bearing, phosphate-free solutions, whereas in the 0.01 m P solutions with F concentrations > 0.02 (2 < mF/mP < 5), the solubility of scheelite was almost the same as in the phosphate-free fluorine-bearing solutions (Fig. 3c). In addition, the fluorine content of the fluorapatite correlated positively with the fluorine concentration at constant phosphate concentration in the solutions (Fig. S6). Reactions (8) and (10) reflect these dissolution processes.

$$5CaWO_{4,(s)} + 3H_2PO_4^- + F^- = Ca_5(PO_4)_3F_{,(s)} + 5WO_4^{2-} + 6H^+ \quad (10)$$
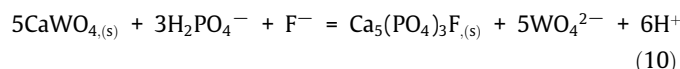
4. Discussion

4.1. The role of F and P in the hydrothermal transport of tungsten

The results of our experiments show that at low pH (<4.5) and elevated fluoride concentration (mF > 0.05), the solubility of scheelite increased as a result of the complexation tungsten as the species $H_3WO_4F_2^-$ (Wang et al., 2021). A similar conclusion can be drawn for experiments conducted with a phosphate concentration of 0.01 at low pH (<4). However, it was not possible to evaluate the nature of the phosphate-bearing tungsten complex. At higher pH (>4.5) fluoride and phosphate ions sequester calcium ions from scheelite to form fluorite and apatite, in the process, greatly increasing the concentration of dissolved tungsten. There are three reasons for this increased concentration. The first relates to the precipitation of fluorite. For example, in a 0.5 m NaCl solution at a pH of 6 and a temperature of 250 °C, the addition of only a small amount of NaF (0.005 m, 87 ppm) increased the concentration of tungsten by a factor of nearly-five from that in the fluorine-free solution (4.15 versus 19.1 ppm). In a 0.03 m NaF solution, the tungsten concentration increased to 313 ppm and in a 0.25 m NaF solution, it increased to 3140 ppm. The second reason for the increased concentration of tungsten relates to the precipitation of apatite. Owing to the deposition of hydroxyapatite from 0.5 m NaCl
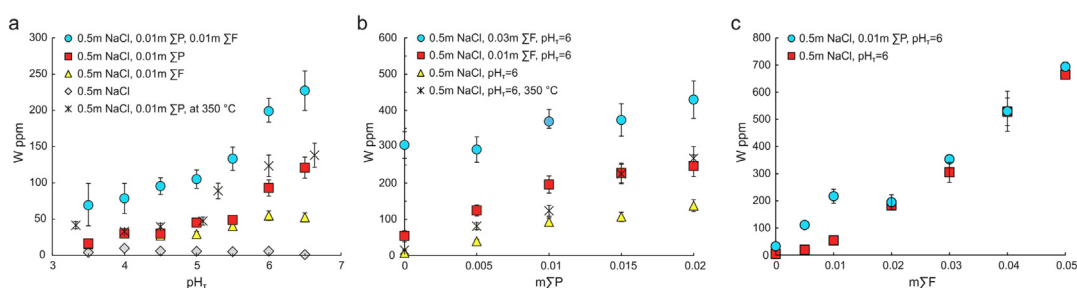

Fig. 3. The solubility of scheelite in solutions with or without fluorine and/or phosphorous. The concentration of tungsten (ppm W) in fluorine-free, fluorine-bearing, phosphorous-bearing and fluorine-phosphorous-bearing at 250 °C and 350 °C (phosphorous-bearing) is shown (a) as a function of pH_T; (b) as a function of the molality of phosphorus; and (c) as a function of the molality of fluorine.
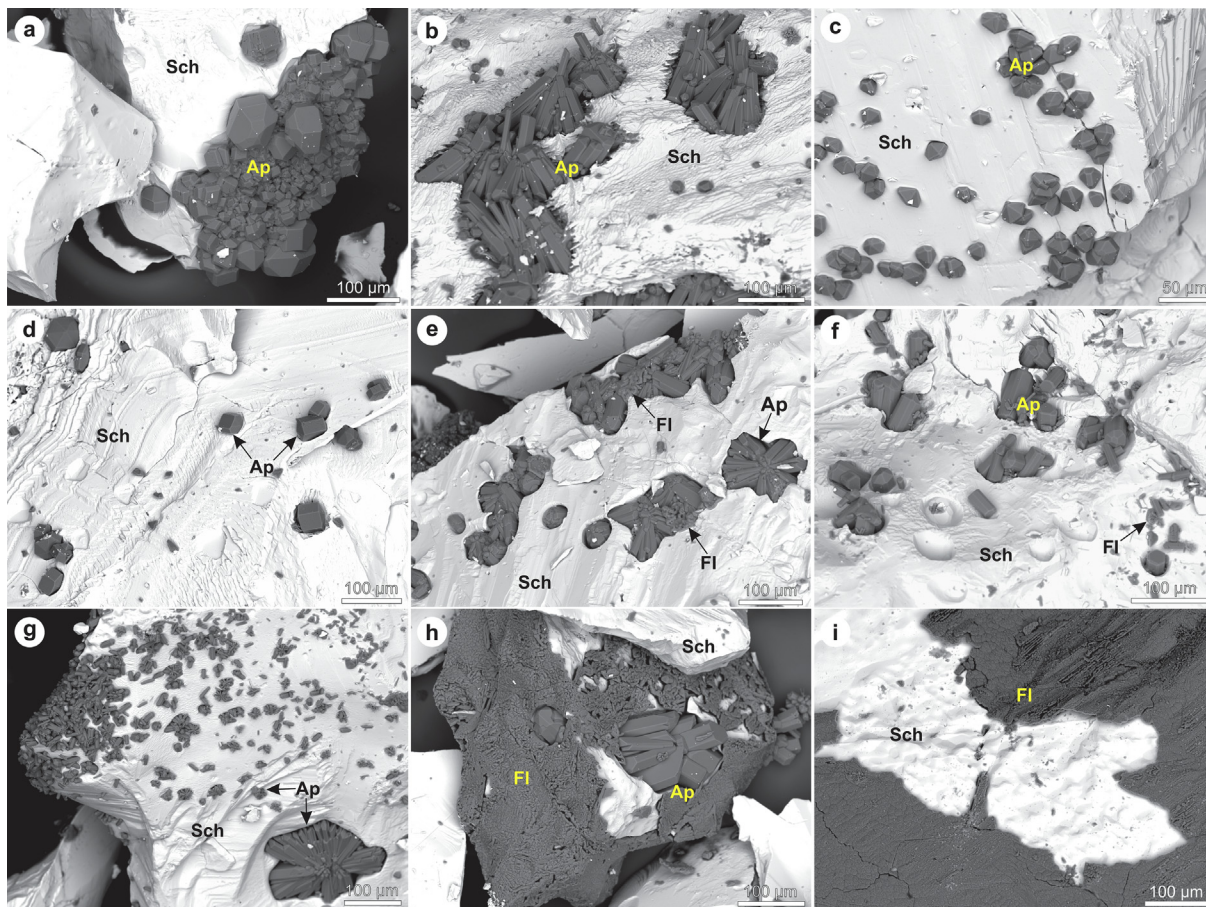
Fig. 4. BSE images showing apatite with or without fluorite crystals on the surface of scheelite. The run products were imaged after solubility experiments at 350 °C (a–b) and 250 °C (c–i) involving a solution containing (a) 0.01 m P at a pH_T of 5.3, (b) and (d) 0.005 m P at a pH_T of 6, (c) 0.01 m P at a pH_T of 4.5, (e) 0.01 m P and 0.01 m F at a pH_T of 5, (f) 0.005 m P and 0.01 m F at a pH_T of 6, (g) 0.02 m P and 0.01 m F at a pH_T of 6, (h) 0.01 m P and 0.03 m F at a pH_T of 6, and (i) 0.01 m P and 0.05 m F at a pH_T of 6.
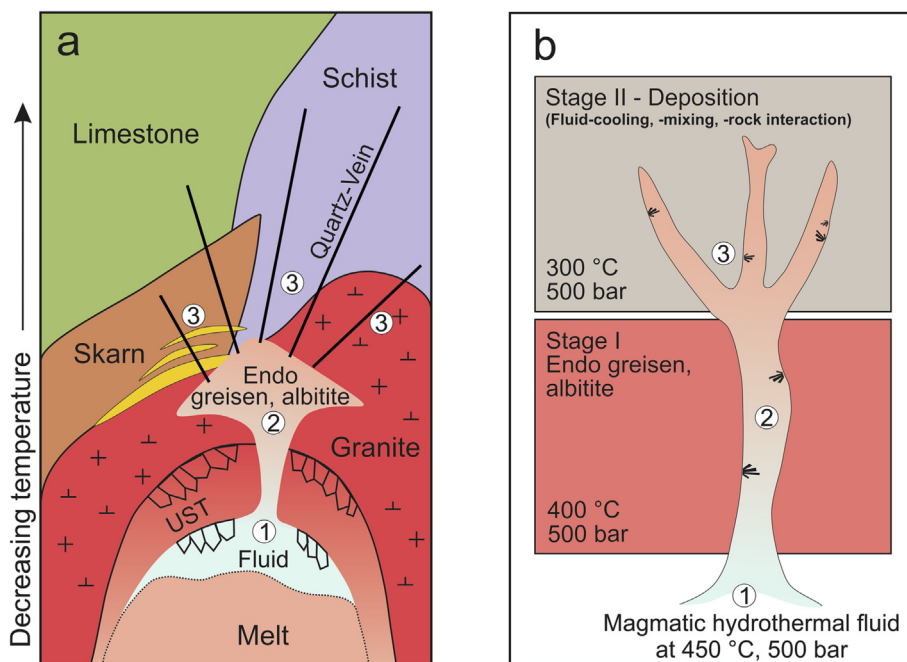
Fig. 5. Cartoons illustrating the geology and the processes of tungsten ore-formation modeled in this study. (a) Illustrates the geology of tungsten deposits. The black lines and yellow colored lenses represent quartz-vein and skarn ores, respectively. The term UST refers to the unidirectional solidification texture of the quartz. (b) Illustrates the stages in the formation of the tungsten deposit represented in the modeling. The numbers ①, ②, and ③ in (a) represent the processes illustrated in (b). (For interpretation of the references to colour in this figure legend, the reader is referred to the web version of this article.)

solutions containing 0.005 to 0.02 m $\sum$P (155 to 620 ppm), at 250 and 350 °C, and a pH > 4.5, the solubility of scheelite increased the dissolved tungsten concentration from 4.2 to 39.6 and from 15.1 to 268 ppm, respectively. Finally, the presence of fluorine promotes the formation of fluorapatite (sequestering more calcium ions than fluorite or hydroxyapatite alone at the same concentration of fluorine or phosphorus), thereby releasing even greater amounts of tungsten to the fluid. Thus, dissolution of scheelite at 250 °C and a pH of 6, in a 0.5 m NaCl solution containing 0.01 m F released ~50 ppm tungsten by precipitating fluorite and in a 0.5 m NaCl solution containing 0.01 m phosphorus released 92.9 ppm tungsten by precipitating hydroxyapatite. In comparison, at the same temperature and pH, a 0.5 m NaCl solution containing 0.01 m phosphorus and 0.01 m fluorine released ~199 ppm tungsten by precipitating fluorapatite. This clearly demonstrates that tungsten concentration resulting from the dissolution of scheelite is maximized in solutions containing both fluorine and phosphorus owing to the combined effects of the deposition of fluorite and fluorapatite. In short, our experimental results show that the presence of fluorite and apatite as gangue minerals in tungsten deposits reflects the important role that fluorine and phosphorus play as ligands in the transport of tungsten and as mediators of the activity of the dissolved calcium that is so essential to the deposition of scheelite.

4.2. Modeling of tungsten hydrothermal transport and deposition

A feature of many large tungsten deposits is the presence of early uneconomic disseminated wolframite in the associated granites (Wang et al., 2003; Breiter et al., 2007; Alekseev et al., 2011; Huang and Jiang, 2014; Xie et al., 2016; Wu et al., 2017; Xie et al., 2018; Monnier et al., 2019; Xiang et al., 2020; Xie et al., 2020). Although early disseminated scheelite is much less common (Noble et al., 1984; Wang et al., 2003), it has been reported for the granites of the giant Zhuxi and Dahutang deposits, in China (Huang and Jiang, 2014; Song et al., 2018a, 2018b, 2018c, 2020). As mentioned in the introduction, remobilization of tungsten from scheelite- and/or wolframite-bearing rocks, including *endo*-skarns, greisens, and albitites, and accompanying fluorite and/or apatite deposition is a very common and important part of the ore-forming process for many tungsten deposits. Moreover, in the case of the Zhuxi deposit, this early scheelite was replaced by fluorite and apatite and is interpreted to have contributed to the main stage scheelite mineralization. In order to further understand how fluorine- and phosphorus-bearing hydrothermal fluids affect the transport and enrichment of tungsten in ore-forming systems, we modeled the behavior of tungsten from the leaching of early uneconomic tungsten mineralization in granites to the formation of high-grade ores of granite-related tungsten deposits using the HCh software package (Shvarov, 2008).

The tungsten deposits referred to in this paper are genetically associated with multi-stage, highly fractionated S-type granitoids and form from hydrothermal fluids released during the crystallization of late-stage magmas (Audétat et al., 2000; Pirajno, 2009). Previous melt- and fluid-inclusion studies of the unidirectional solidification textured (UST) quartz and pegmatites in sn-W-(Nb-Ta-F) deposits have reported relatively high contents of iron (2121–31646 ppm), calcium (0–7615 ppm), phosphorus (0–1138 ppm), and tungsten (10–1415 ppm) (Webster et al., 1997; Audétat et al., 2000; Zajacz et al., 2008). The fluorine content of the fluids has been shown to be in the range ~800 to ~6500 ppm (Vasyukova and Williams-Jones, 2018). These magmatic hydrothermal fluids are carbonic, supercritical (4.5–15 wt% NaCl equivalent) and are commonly trapped at ~450 °C and ~500 bar (Zajacz et al., 2008). The ores, however, have been interpreted to form at temperatures between 250 and 350 °C via fluid-

cooling, fluid-mixing, or fluid-rock interaction. They are commonly associated with apatite and fluorite in *exo*-greisens, quartz veins, skarns, and to a lesser extent in porphyries, and were preceded by the formation of *endo*-greisens, *endo*-skarns and albitites (Pirajno, 2009; Song et al., 2020). Their geological relationships are illustrated in Fig. 5.

In our models, a magmatic-hydrothermal fluid (stable at 450 °C) was reacted in 250 g aliquots with 1 Kg of tungsten-bearing granite (0.001 m wolframite and 0.001 m scheelite; ~368 ppm tungsten) at 400 °C and 500 bar to recreate the *endo*-greisen and albitite (Stage I) (Fig. 5). The same post-reaction fluid aliquots were then used to simulate tungsten mineral deposition in three scenarios: (1) cooling at 300 °C and 500 bar, (2) mixing of a 400 °C ore fluid with a 200 °C meteoric water, and (3) interaction of the 300 °C ore fluid with the host-rock (Stage II). In the cooling model, the reacted fluid from Stage I (400 °C) was cooled to 300 °C and 500 bar. The fluid-mixing model involved mixing the ore fluid from Stage I in a 1:1 ratio with the meteoric water (a 0.2 m NaCl solution containing 0.0035 mol of CO_2) that had equilibrated with limestone, schist, granite, and skarn at 200 °C and 500 bar (four models). The fluid-rock interaction modeling involved reacting the ore fluid from Stage I with these same rock types (limestone, schist, granite, or skarn) at 300 °C and 500 bar. The following is the composition of the magmatic-hydrothermal fluid used in the modeling: iron (5600 ppm), calcium (400 ppm), phosphorus (155 ppm), tungsten (80 ppm), and fluorine (3800 ppm). For the purpose of the modeling, the oxygen fugacity of the fluid was assumed to correspond to that of the quartz-fayalite-magnetite (QFM) buffer and the XCO_2 to be 0.001 (Wood and Samson, 2000). For comparison, a fluorine- and phosphorus-free equivalent of the above fluid was also allowed to undergo the above two stages modeling. The compositions of the magmatic hydrothermal fluid, host rocks for the fluid-rock interaction (Polya, 1989; Lu et al., 2003; Guo et al., 2012), and the meteoric fluid for fluid-mixing are provided in Table 2. For simplicity, ferberite (FeWO$_4$) was taken to represent wolframite. The sources of the data for the minerals and aqueous species are listed in Table S3.

During Stage I, interaction of the fluorine-phosphorus-bearing magmatic-hydrothermal fluid with tungsten-bearing granite led to the progressive replacement of the major rock-forming minerals, microcline, and annite, by albite, then by quartz, fluorite, phlogopite and fluorapatite with increasing fluid/rock ratio and, eventually topaz, which replaced fluorite (Fig. 6a). This process reflects the alteration of the granite to form albitite and *endo*-greisen. The ferberite initially in the granite was replaced by scheelite and then was gradually dissolved together with initial scheelite, replaced by ferberite at a fluid/rock ratio between 1.5 and 3.5, and finally dissolved completely at a fluid/rock ratio of 55. The pH climbed sharply from an initial value of 4.2 to a value of 5.5–6 (Fig. 6b). The concentration of W decreased sharply from an initial value of 4.4×10^{-4} m to 2.0×10^{-6} m and then increased to 0.001 m between a fluid/rock ratio of 0.25 and 1.25. The increase in W concentration corresponded to a sharp drop in the concentration of Ca due to the crystallization of fluorite and to a lesser extent fluorapatite, and the replacement of ferberite by scheelite. At higher fluid/rock ratios, the concentration of W gradually decreased to its initial value with complete leaching of the scheelite from the granite.

Cooling of the post-reaction fluorine-phosphorus-bearing fluid at 300 °C, and its mixing with meteoric water during Stage II produced very similar results (Fig. 6e and 6f; Fig. S7a–S7c). They show that mixing of the magmatic-hydrothermal fluid (400 °C in a magmatic-hydrothermal/meteoric fluid ratio of 1) with a meteoric fluid (200 °C) that had equilibrated with its host rocks (e.g., limestone, schist, granite, and skarn) has little effect on the composition of the ore-forming fluid and the precipitation of tungsten minerals.

Table 2

The composition of the magmatic hydrothermal fluid, the meteoritic fluid, and the host rocks used in the models.

Magmatic hydrothermal fluid at 450 °C and 500 bar[a]					The meteoritic fluid after equilibration with the host rocks at X_{CO2} = 0.001, 200 °C, and 500 bar[b]			
	F-P-bearing fluid		F- and P-free fluid			Granite	Schist	Limestone	Skarn
	mol/kg	ppm	mol/kg	ppm		mol/kg	mol/kg	mol/kg	mol/kg
NaCl	3	69,000 (ΣNa)	3	69,000 (ΣNa)	NaCl	1.90E−01	1.92E−01	2.00E−01	1.97E−01
KCl	0.2	7800 (ΣK)	0.2	7800 (ΣK)	KCl	7.24E−03	7.20E−03	0	0
MgCl$_2$	0.02	480 (ΣMg)	0.02	480 (ΣMg)	MgCl$_2$	3.04E−06	2.46E−04	2.72E−04	7.09E−06
Al$_2$O$_3$	0.025	1350 (ΣAl)	0.0015	79 (ΣAl)	Al(OH)$_3$	3.20E−06	9.60E−07	0	3.00E−06
CaCl$_2$	0.01	400 (ΣCa)	0.01	400 (ΣCa)	CaCl$_2$	1.79E−03	0	6.51E−04	1.92E−03
FeCl$_2$	0.1	5600 (ΣFe)	0.1	5600 (ΣFe)	FeCl$_2$	2.17E−07	6.66E−06	0	2.31E−07
NaF	0.2	3800 (ΣF)	0	0	SiO$_2$	2.65E−03	2.60E−03	0	2.63E−03
NaH$_2$PO$_4$	0.005	155 (ΣP)	0	0	NaHCO$_3$	2.36E−04	3.25E−05	4.10E−04	2.34E−04
H$_2$S	0.016	513 (ΣS)	0.016	513 (ΣS)	NaOH	2.35E−05	0	2.71E−06	1.55E−06
As$_2$O$_3$	0.003	450 (ΣAs)	0.003	450 (ΣAs)	pH 200 °C	6.13	5.32	6.42	6.08
Quartz	0.02	1200 (ΣSi)	0.017	1040 (ΣSi)					
WO$_3$	0.00044	80 (ΣW)	0.00044	80 (ΣW)					
HCl	0.16		0.01188						
pH 450 °C	5.04		5.046						

Granite[c]		Schist[c]		Limestone		Skarn[c]	
Major elements (wt.%)							
SiO$_2$	74.79	SiO$_2$	71.5			SiO$_2$	41.9
Al$_2$O$_3$	13.43	Al$_2$O$_3$	15.0			Al$_2$O$_3$	7.35
Fe$_2$O$_3^T$	1.58	Fe$_2$O$_3^T$	6.16			FeO^T	15.4
CaO	0.75	CaO	0.06			CaO	29.8
Na$_2$O	3.58	Na$_2$O	1.44			MgO	3.66
K$_2$O	4.64	K$_2$O	2.04				
MgO	0.13	MgO	2.17				
Total	99.08	Total	98.37			Total	98.11
Mineral composition (g)							
Microcline	244	Daphnite	110	Calcite	900	Diopside	181
Albite	303	Albite	40	Dolomite	100	Hedenbergite	104
Anorthite	37	Paragonite	119			Almandine	36
Annite	45	Quartz	496			Pyrope	36
Quartz	367	Muscovite	173			Grossular	300
Phlogopite	4	Anorthite	3			Andradite	343
		Clinochlore	59				
Total	1000	Total	1000	Total	1000	Total	1000

Note:

 [a] The composition of the magmatic hydrothermal fluid is based on the compositions of fluid inclusions associated with melt inclusions from UST quartz and pegmatite in a sn-W-(Nb-Ta-F) deposit (Audétat et al., 2000; Zajacz et al., 2008). The fluorine content of the fluid was evaluated from the measurements of the concentration of fluorine in fluid inclusions in a highly fractionated granite (Vasyukova and Williams-Jones, 2018).

[b] The composition of the meteoritic fluid is from a fluid containing 0.2 m NaCl and 0.0035 mol of CO$_2$ (XCO$_2$ = 0.001) that had equilibrated with limestone, schist, granite, or skarn at 200 °C and 500 bar.

[c] The composition of the granite is that of garnet-bearing fine-grained porphyritic biotite granite from the Xihuashan deposit, China (Guo et al., 2012). The composition of the schist is that of the Schist CG-U from the Panasqueira deposit, Portugal (Polya, 1989). The skarn consists of pyroxene (30 wt%, D14a) and garnet (70 wt%, S9326) and is from Shizhuyuan deposit, China (Lu et al., 2003). The mineral compositions of the host rocks were calculated from the its major element composition using the relationship X = B/A where X is a vector of the proportions of the different minerals, B is a matrix of mineral compositions and A is a vector corresponding to the bulk rock chemical composition. The formulae and sources of thermodynamic data for the minerals are listed in Table S3.

The Ca and Fe concentrations and the pH in both cases were mainly inherited from the magmatic-hydrothermal fluid. In the fluid-schist interaction model (Fig. 6g), the initially high Ca concentration in the fluid relative to that of Fe triggered the precipitation of scheelite at a fluid/rock ratio between 0.25 and 0.5, whereas at higher fluid/rock ratios the decrease in Ca concentration led to the precipitation of ferberite in place of scheelite. As might be expected, in the fluid-limestone interaction model, the Ca concentration was consistently higher than that of Fe, and consequently scheelite was the only tungsten mineral to precipitate between a fluid/rock ratio of 0.25 and 60 (Fig. 6h). The pH of the fluid was also much higher than in the fluid-schist interaction model, ~6 versus ~4. At very high fluid/rock ratios (>60), leaching of calcite in the limestone led to the precipitation of fluorite and apatite and a sharp decrease in the Ca/Fe ratio, promoting the replacement of scheelite by ferberite. The results of the fluid-granite and fluid-skarn interaction models are very similar to those of the fluid-

schist and fluid-limestone interaction models, respectively (Fig. S7d–S7e).

In the fluorine-phosphorus-free system, actinolite, hedenbergite, and corundum formed in association with albitite and *endo*greisen alteration (Fig. 6c). The ferberite initially in the granite was replaced by scheelite. The amount of scheelite increased from 0.002 m to 0.02 m as the fluid/rock ratio increased from 0.25 to 52, and then decreased to 0.0062 m at a fluid/rock ratio of 100. As in the fluorine-phosphorus-bearing system, the Fe concentration was maintained at a high value and decreased from ~0.3 m to the initial value 0.1 m as the fluid/rock ratio increased from 0.25 to 100. The pH climbed from the initial value of 3.6 to a value of 5.5, then increased to 6.09 (Fig. 6d), and was accompanied by a sharp decrease in the concentration of W from an initial value of 4.4×10^{-4} m to 1.8×10^{-6} m and then an increase to 4.5×10^{-6} m between a fluid/rock ratio of 0.25 and 8. At higher fluid/rock ratios, the concentration of W increased steeply to 7.2×10^{-4} m,
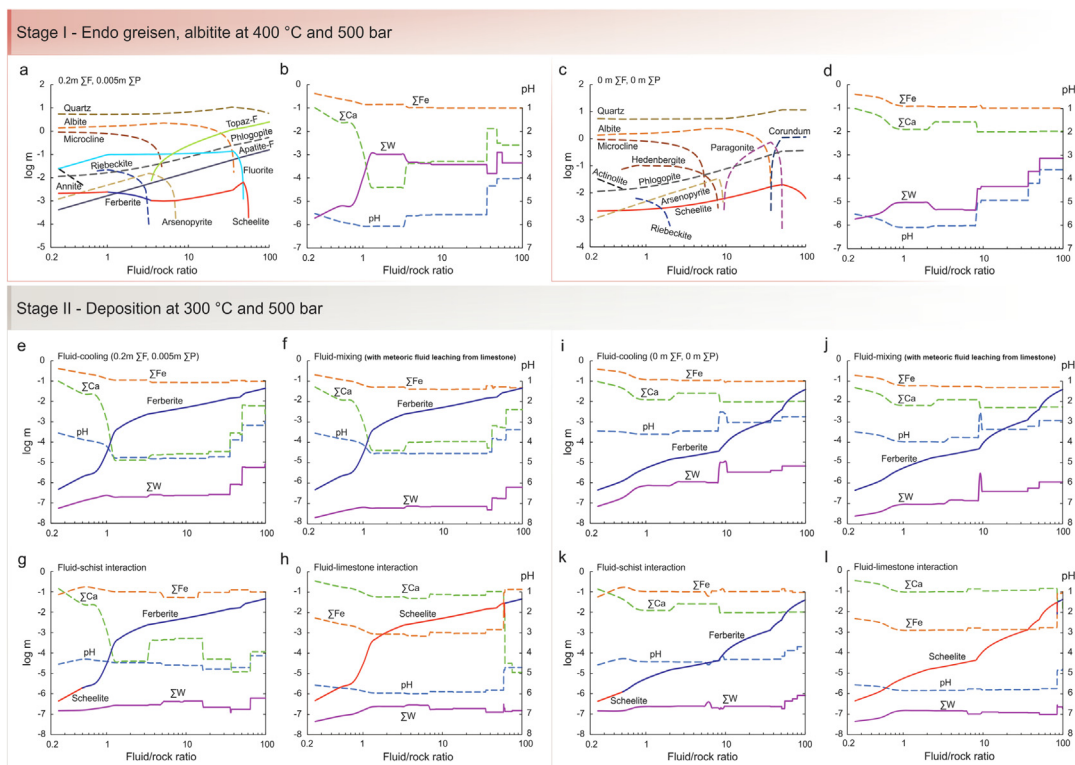
Fig. 6. Diagrams showing the simulated changes in the mineralogy and fluid chemistry as a function of the fluid/rock ratio. The changes are after reaction of 250 g aliquots of fluid with 1 kg of scheelite-bearing granite at 400 °C and 500 bar (a–d), followed by those occurring in response to cooling, fluid mixing and fluid-rock reaction during interaction of 250 g aliquots of the fluid from Stage I with 1 Kg of rock at 300 °C and 500 bar (e–l). (a) the moles of minerals produced from a fluid initially containing 0.2 m $\sum$F and 0.01 m $\sum$P, (b) the pH and molality of Ca, Fe and W in this fluid. (e–h) the moles of tungsten minerals produced from and the concentrations of Ca, Fe and W in the fluid from Stage I (e) on cooling, (f) on mixing with a meteoric fluid that had equilibrated with its host rocks, (g) on interaction with schist, and (h) on interaction with limestone. (c and d) and (i, j, k, and l) illustrate the results with a F- and P-free fluid corresponding to those of (a and b) and (e, f, g, and h). The results of these modeling are reported in the file of Research Data enclosed as Supplementary Material.

due to a corresponding decrease in pH from 6 to 3.6. The concentration of tungsten in the reacted fluid at a pH > 4 and 400 °C is 8–220 times lower than with a fluorine-phosphorus-bearing fluid at a fluid/rock ratio between 1 and 36. The results of the Stage II models for fluid-cooling and -mixing are similar (Fig. 6i and 6j; Fig. S7f–S7h). As in the fluorine-phosphorus-bearing system, the Ca and Fe concentrations were mainly inherited from the initial fluid, and the only tungsten mineral to precipitate was ferberite. In contrast, in the fluid-rock interaction model, the Ca and Fe concentrations and pH of the fluid were largely a product of the nature of the host rock. Scheelite precipitated as a result of reaction of the fluid with limestone and skarn, whereas ferberite precipitated on its interaction with granite and schist (Fig. 6k and 6l; Fig. S7i and S7j). We also note that the amount of tungsten mineral that precipitated was the same in each of the four interaction models. This indicates that fluid-cooling is probably the primary control on tungsten mineral precipitation under the conditions of our modeling. Nevertheless, we do not rule out the possibility that fluid-mixing and fluid-rock interaction can supply Ca and Fe and/or neutralize the pH of the ore-forming fluids all of which are critical for tungsten mineral precipitation. The most important finding of the modeling of deposition, however, is that the amount of tungsten mineral precipitated in the fluorine-phosphorus-free fluid was 10–125 times lower than in the corresponding models involving a fluorine-phosphorus-bearing fluid at a pH > 4.

4.3. Implications for ore genesis

Tungsten has a concentration of ∼1.9 ppm (Rudnick and Gao, 2003) in the upper crust and has to be enriched by a factor of

500–800 to reach a bulk mineable grade (0.12–0.20 wt% of WO₃, 950–1,580 ppm of W), and by a factor of 2,000–20,000 times to generate a vein-type deposit (0.5–5 wt% of WO₃, 3,965–39,650 ppm of W; Schmidt et al., 2012; Brown and Pitfield, 2014). Although the fractionation of residual F-, B-, and P-rich melts can enrich the tungsten content by 20–100 times over its upper crustal content, i.e., to a concentration of 40–200 ppm (Audétat et al., 2000; Zajacz et al., 2008), a further 6–>20 times enrichment is required to form an economic tungsten deposit. A way to achieve this enrichment is through remobilization of pre-existing early uneconomic low-grade tungsten mineralization.

The results of our experiment results show that a fluorine- and/or phosphorus-bearing hydrothermal fluid (0.05–0.25 m$\sum$F and/or 0.01 m$\sum$P) can transport from 100 to 1000 times more tungsten in a calcium-bearing fluid at a pH between 4 and 7 than a F- and P-free fluid. In our models, a fluorine- and phosphorus-bearing magmatic hydrothermal fluid (0.2 m$\sum$F and 0.005 m$\sum$P) leached tungsten from tungsten-bearing granite during the formation of albite and *endo*-greisen, and on cooling deposited tungsten minerals. The solubility of tungsten in the reacted fluid at a pH > 4 and 400 °C and the mole of tungsten minerals precipitated at 300 °C are, respectively, 8–220 times and 10–125 times higher than with a fluorine-phosphorus-free fluid at a fluid/rock ratio between 1 to ∼40. These results show that fluorine- and phosphorus-bearing fluids have a great capacity to be enriched in tungsten during high-temperature alteration at depth and form high-grade low-temperature vein-type deposits at high crustal levels.

Apatite and fluorite are common minerals in large tungsten deposits, particularly in the aplites and albitites, which precede tungsten mineralization (Rasmussen et al., 2011; Song et al.,

2020). This indicates that the late-stage magmas and associated fluids are P- and F-rich. As precipitation of apatite and fluorite from these fluids promotes the dissolution of scheelite, such high concentrations of P and F may be key to the remobilization of tungsten in ore-forming concentrations. Thus, it is noteworthy that large tungsten deposits are commonly associated with multiple stages of intrusion and exsolution of magmatic-hydrothermal fluids (Polya, 1989; Jingwen et al., 1996; Lu et al., 2003; Breiter et al., 2017; Song et al., 2018a; 2018c; Monnier et al., 2020). Consequently, there is an opportunity for repeated dissolution of early tungsten minerals by fluorine- and phosphorus-rich fluids and the progressive upgrading of the tungsten mineralization to levels sufficient to form giant ore deposits. Indeed, the multiple stages of scheelite associated with fluorite and/or apatite reported for deposits such Zhuxi and Dahutang may record such tungsten remobilization and enrichment (Huang and Jiang, 2014; Song et al., 2018a, 2018b; 2018c, 2020). We, therefore, conclude that a key to forming large, high-grade scheelite deposits is a long-term synergy between the tungsten-enriching effects (scheelite dissolution) of apatite/fluorite deposition from an F- and/or P-rich fluid and the subsequent interaction of this fluid with a calcium-rich source.

5. Conclusions

This contribution successfully addresses the issue of why large tungsten deposits are commonly associated with fluorine- and phosphorus-enriched magmas and ore-forming fluids. Specifically, it shows how the competition of gangue and ore minerals for components dissolved in hydrothermal fluids can play a pivotal role in determining whether an ore deposit will form, an aspect of ore-genesis that is rarely considered. In the case of tungsten deposits, the competition for calcium ions, by apatite and fluorite greatly increases the solubility of scheelite. Thus, the fluorine and phosphorus concentrations as well as pH are key factors that affect the transport and deposition of tungsten in hydrothermal systems which, if they act synergistically, can highly enrich tungsten from low-grade mineralization to the ore-forming fluids and lead to the formation of high-grade deposits. The same observations may also apply to other metals, for which there is potential for competition between ore and gangue minerals for components of the mineralizing hydrothermal fluid, and thus future studies should consider this possibility in refining or developing new models of ore genesis for deposit types where this may be the case.

Declaration of Competing Interest

The authors declare that they have no known competing financial interests or personal relationships that could have appeared to influence the work reported in this paper.

Acknowledgments

Appendix A. Supplementary material

The supplementary material for this article includes supplementary figures and tables and a file of Research Data. The file of supplementary figures and tables comprises seven figures (Figs. S1–S7) and three tables (Tables S1–S3). The file of Research Data consists of eighteen excel files displaying the results of modeling illustrated in Figs. 6 and S7. Supplementary material to this article can be found online at https://doi.org/10.1016/j.gca.2023.02.001.

References

Alekseev, V.I., Gembitskaya, I.M., Marin, Y.B., 2011. Wolframoixiolite and niobian ferberite from zinnwaldite granitic rocks of the Chukchi Peninsula. Geol. Ore Depos. 53, 639–648.

Audétat, A., Günther, D., Heinrich, C.A., 1998. Formation of a Magmatic-Hydrothermal Ore Deposit: Insights with LA-ICP-MS Analysis of Fluid Inclusions. Science 279, 2091–2094.

Audétat, A., Gunther, D., Heinrich, C.A., 2000. Magmatic-hydrothermal evolution in a fractionating granite: A microchemical study of the Sn-W-F-mineralized Mole Granite (Australia). Geochim. Cosmochim. Acta 64, 3373–3393.

Bailly, L., Grancea, L., Kouzmanov, K., 2002. Infrared microthermometry and chemistry of wolframite from the Baia Sprie epithermal deposit, Romania. Econ. Geol. Bull. Soc. Econ. Geol. 97, 415–423.

Breiter, K., Škoda, R., Uher, P., 2007. Nb-Ta-Ti-W-Sn-oxide minerals as indicators of a peraluminous P- and F-rich granitic system evolution: Podlesí, Czech Republic. Mineral. Petrol. 91, 225–248.

Breiter, K., Ďurišová, J., Hrstka, T., Korbelová, Z., Hložková Vaňková, M., Vašinová Galiová, M., Kanický, V., Rambousek, P., Knésl, I., Dobeš, P., Dosbaba, M., 2017. Assessment of magmatic vs. metasomatic processes in rare-metal granites: A case study of the Cínovec/Zinnwald Sn–W–Li deposit. Central Europe. Lithos 292–293, 198–217.

Brown, T., Pitfield, P., 2014. Tungsten. Critical Metals Handbook, 385–413.

Brugger, J., Liu, W., Etschmann, B., Mei, Y., Sherman, D.M., Testemale, D., 2016. A review of the coordination chemistry of hydrothermal systems, or do coordination changes make ore deposits? Chem. Geol. 447, 219–253.

Campbell, A.R., Robinsoncook, S., 1987. Infrared fluid inclusion microthermometry on coexisting wolframite and quartz. Econ. Geol. 82, 1640–1645.

Carocci, E., Truche, L., Cathelineau, M., Caumon, M.-C., Bazarkina, E.F., 2022. Tungsten (VI) speciation in hydrothermal solutions up to 400°C as revealed by in-situ Raman spectroscopy. Geochim. Cosmochim. Acta 317, 306–324.

Choi, W., Park, C., Song, Y., 2020. Multistage W-mineralization and magmatic-hydrothermal fluid evolution: Microtextural and geochemical footprints in scheelite from the Weondong W-skarn deposit, South Korea. Ore Geol. Rev. 116, 103219.

Ding, T., Ma, D., Lu, J., Zhang, R., 2018. Garnet and scheelite as indicators of multi-stage tungsten mineralization in the Huangshaping deposit, southern Hunan province. China. Ore Geol. Rev. 94, 193–211.

Graupner, T., Kempe, U., Dombon, E., Pätzold, O., Leeder, O., Spooner, E.T.C., 1999. Fluid regime and ore formation in the tungsten(–yttrium) deposits of Kyzyltau (Mongolian Altai): evidence for fluid variability in tungsten–tin ore systems. Chem. Geol. 154, 21–58.

Guo, C.L., Chen, Y.C., Zeng, Z.L., Lou, F.S., 2012. Petrogenesis of the Xihuashan granites in southeastern China: Constraints from geochemistry and in-situ analyses of zircon U-Pb-Hf-O isotopes. Lithos 148, 209–227.

Han, R., Ren, T., Li, W., Huang, J., Wang, L., Huang, R., Yuan, Y., 2020. Discovery of the large-scale Huangtian scheelite deposit and implications for the structural control of tungsten mineralization in southeastern Yunnan, south China. Ore Geol. Rev. 121, 103480.

Hedenquist, J.W., Lowenstern, J.B., 1994. The role of magmas in the formation of hydrothermal ore-deposits. Nature 370, 519–527.

Heinrich, C.A., 1990. The chemistry of hydrothermal tin(-tungsten) ore deposition. Econ. Geol. 85, 457–481.

Helgeson, H.C., Kirkham, D.H., 1974. Theoretical prediction of the thermodynamic behavior of aqueous electrolytes at high pressures and temperatures; I, Summary of the thermodynamic/electrostatic properties of the solvent. Am. J. Sci. 274, 1089–1198.

Helgeson, H.C., Kirkham, D.H., Flowers, G.C., 1981. Theoretical prediction of the thermodynamic behavior of aqueous electrolytes by high pressures and temperatures; IV, Calculation of activity coefficients, osmotic coefficients, and apparent molal and standard and relative partial molal properties to 600 degrees C and 5kb. Am. J. Sci. 281, 1249–1516.

Holland, T.J.B., Powell, R., 2011. An improved and extended internally consistent thermodynamic dataset for phases of petrological interest, involving a new equation of state for solids. J. Metamorph. Geol. 29, 333–383.

Huang, L.-C., Jiang, S.-Y., 2014. Highly fractionated S-type granites from the giant Dahutang tungsten deposit in Jiangnan Orogen, Southeast China: geochronology, petrogenesis and their relationship with W-mineralization. Lithos 202–203, 207–226.

Jingwen, M., Hongyan, L., Shimazaki, H., Raimbault, L., Guy, B., 1996. Geology and Metallogeny of the Shizhuyuan Skarn-Greisen Deposit, Hunan Province, China. Int. Geol. Rev. 38, 1020–1039.

Kestin, J., Sengers, J.V., Kamgar-Parsi, B., Sengers, J.M.H.L., 1984. Thermophysical Properties of Fluid H_2O. J. Phys. Chem. Ref. Data 13, 175–183.

Kiseleva, I., Ogorodova, L., Khodakovskiy, I., Khodakovskij, I., 1980. Thermodynamic properties of scheelite $CaWO_4$ and the tungstate ion. Geochem. Int. 17, 87–92.

Lecumberri-Sanchez, P., Vieira, R., Heinrich, C.A., Pinto, F., Wälle, M., 2017. Fluid-rock interaction is decisive for the formation of tungsten deposits. Geology 45, 579–582.

Legros, H., Richard, A., Tarantola, A., Kouzmanov, K., Mercadier, J., Vennemann, T., Marignac, C., Cuney, M., Wang, R.-C., Charles, N., Bailly, L., Lespinasse, M.-Y., 2019. Multiple fluids involved in granite-related W-Sn deposits from the world-class Jiangxi province (China). Chem. Geol. 508, 92–115.

Lu, H.Z., Liu, Y.M., Wang, C.L., Xu, Y.Z., Li, H.Q., 2003. Mineralization and fluid inclusion study of the Shizhuyuan W-Sn-Bi-Mo-F skarn deposit, Hunan province, China. Econ. Geol. Bull. Soc. Econ. Geol. 98, 955–974.

Marshall, W.L., Franck, E., 1981. Ion product of water substance, 0–1000 C, 1–10,000 bars New International Formulation and its background. J. Phys. Chem. Ref. Data 10, 295–304.

Migdisov, A.A., Williams-Jones, A.E., 2007. An experimental study of the solubility and speciation of neodymium (III) fluoride in F-bearing aqueous solutions. Geochim. Cosmochim. Acta 71, 3056–3069.

Monnier, L., Salvi, S., Melleton, J., Bailly, L., Béziat, D., de Parseval, P., Gouy, S., Lach, P., 2019. Multiple Generations of Wolframite Mineralization in the Echassieres District (Massif Central, France). Minerals 9, 637.

Monnier, L., Salvi, S., Jourdan, V., Sall, S., Bailly, L., Melleton, J., Béziat, D., 2020. Contrasting fluid behavior during two styles of greisen alteration leading to distinct wolframite mineralizations: The Echassières district (Massif Central, France). Ore Geol. Rev. 124, 103648.

Moura, A., Doria, A., Neiva, A.M.R., Gomes, C.L., Creaser, R.A., 2014. Metallogenesis at the Carris W-Mo-Sn deposit (Geres, Portugal): Constraints from fluid inclusions, mineral geochemistry, Re-Os and He-Ar isotopes. Ore Geol. Rev. 56, 73–93.

Ni, P., Wang, X.-D., Wang, G.-G., Huang, J.-B., Pan, J.-Y., Wang, T.-G., 2015. An infrared microthermometric study of fluid inclusions in coexisting quartz and wolframite from Late Mesozoic tungsten deposits in the Gannan metallogenic belt, South China. Ore Geol. Rev. 65, 1062–1077.

Ni, P., Li, W.-S., Pan, J.-Y., Cui, J.-M., Zhang, K.-H., Gao, Y., 2022. Fluid Processes of Wolframite-Quartz Vein Systems: Progresses and Challenges. Minerals 12, 237.

Noble, S., Spooner, E.T., Harris, F., 1984. The Logtung large tonnage, low-grade W (scheelite)-Mo porphyry deposit, south-central Yukon Territory. Econ. Geol. 79, 848–868.

Oelkers, E.H., Helgeson, H.C., 1990. Triple-ion anions and polynuclear complexing in supercritical electrolyte solutions. Geochim. Cosmochim. Acta 54, 727–738.

Oelkers, E.H., Helgeson, H.C., 1991. Calculation of activity coefficients and degrees of formation of neutral ion pairs in supercritical electrolyte solutions. Geochim. Cosmochim. Acta 55, 1235–1251.

Pan, J.Y., Ni, P., Wang, R.C., 2019. Comparison of fluid processes in coexisting wolframite and quartz from a giant vein-type tungsten deposit, South China: Insights from detailed petrography and LA-ICP-MS analysis of fluid inclusions. Am. Miner. 104, 1092–1116.

Pearson, R.G., 1963. Hard and Soft Acids and Bases. J. Am. Chem. Soc. 85, 3533–3539.

Piccoli, P.M., Candela, P.A., 2002. Apatite in Igneous Systems. Rev. Miner. Geochem. 48, 255–292.

Pirajno, F., 2009. Hydrothermal processes and mineral systems. Springer, Berlin, p. 1250.

Pokrovski, G.S., Kara, S., Roux, J., 2002. Stability and solubility of arsenopyrite, FeAsS, in crustal fluids. Geochim. Cosmochim. Acta 66, 2361–2378.

Polya, D.A., 1989. Chemistry of the main-stage ore-forming fluids of the Panasqueira W-Cu(Ag)-Sn deposit, Portugal - implications for models of ore genesis. Econ. Geol. 84, 1134–1152.

Qiu, Y., Wang, X., Lu, J., Chou, I.M., Wan, Y., Zhang, R., Zhang, W., Sun, R., 2022. In situ observations of tungsten speciation and partitioning behavior during fluid exsolution from granitic melt. Sci. Bull. 67, 2358–2368.

Rasmussen, K.L., Lentz, D.R., Falck, H., Pattison, D.R.M., 2011. Felsic magmatic phases and the role of late-stage aplitic dykes in the formation of the world-class Cantung Tungsten skarn deposit, Northwest Territories. Canada. Ore Geol. Rev. 41, 75–111.

Robie, R.A., Hemingway, B.S., 1995. Thermodynamic properties of minerals and related substances at 298.15 K and 1 bar (10^5 pascals) pressure and at higher temperatures.

Roy-Garand, A., Adlakha, E., Hanley, J., Elongo, V., Lecumberri-Sanchez, P., Falck, H., Boucher, B., 2022. Timing and sources of skarn mineralization in the Canadian Tungsten Belt: revisiting the paragenesis, crystal chemistry and geochronology of apatite. Miner. Depos. 57, 1391–1413.

Rudnick, R.L., Gao, S., 2003. Composition of the continental crust. Treatise geochem. 3, 1–64.

Samson, I.M., 1990. Fluid evolution and mineralization in a subvolcanic granite stock; the Mount Pleasant W-Mo-Sn deposits, New Brunswick. Canada. Econ. Geol. 85, 145–163.

Schmidt, S., Berghau, W., Hutten, A., 2012. From deposit to concentrate: The basics of tungsten mining Part 1: Project generation and project development. Int. Tungsten Ind. Assoc 4, 1–20.

Schwartz, M., Surjono, 1990. Greisenization and albitization at the Tikus tin-tungsten deposit, Belitung, Indonesia. Econ. Geol. 85, 691–713.

Seward, T.M., Williams-Jones, A.E., Migdisov, A.A., 2014. The Chemistry of Metal Transport and Deposition by Ore-Forming Hydrothermal Fluids. 29–57.

Shock, E.L., Sassani, D.C., Willis, M., Sverjensky, D.A., 1997. Inorganic species in geologic fluids: Correlations among standard molal thermodynamic properties of aqueous ions and hydroxide complexes. Geochim. Cosmochim. Acta 61, 907–950.

Shvarov, Y.V., 2008. HCh: New potentialities for the thermodynamic simulation of geochemical systems offered by windows. Geochem. Int. 46, 834–839.

Soloviev, S.G., Kryazhev, S.G., 2017. Geology, mineralization, and fluid inclusion characteristics of the Skrytoe reduced-type W skarn and stockwork deposit, Sikhote-Alin, Russia. Miner. Depos. 52, 903–928.

Song, S., Mao, J., Xie, G., Yao, Z., Chen, G., Rao, J., Ouyang, Y., 2018a. The formation of the world-class Zhuxi scheelite skarn deposit: Implications from the petrogenesis of scheelite-bearing anorthosite. Lithos 312–313, 153–170.

Song, S., Mao, J., Zhu, Y., Yao, Z., Chen, G., Rao, J., Ouyang, Y., 2018b. Partial-melting of fertile metasedimentary rocks controlling the ore formation in the Jiangnan porphyry-skarn tungsten belt, south China: A case study at the giant Zhuxi W-Cu skarn deposit. Lithos 304–307, 180–199.

Song, S., Mao, J., Xie, G., Jian, W., Chen, G., Rao, J., Ouyang, Y., 2020. Petrogenesis of Scheelite-Bearing Albitite as an Indicator for the Formation of a World-Class Scheelite Skarn Deposit: A Case Study of the Zhuxi Tungsten Deposit. Econ. Geol. 116, 91–121.

Song, W.L., Yao, J.M., Chen, H.Y., Sun, W.D., Ding, J.Y., Xiang, X.K., Zuo, Q.S., Lai, C.K., 2018c. Mineral paragenesis, fluid inclusions, H-O isotopes and ore-forming processes of the giant Dahutang W-Cu-Mo deposit, South China. Ore Geol. Rev. 99, 116–150.

Sverjensky, D.A., Shock, E.L., Helgeson, H.C., 1997. Prediction of the thermodynamic properties of aqueous metal complexes to 1000°C and 5 kb. Geochim. Cosmochim. Acta 61, 1359–1412.

Tagirov, B.R., Zotov, A.V., Akinfiev, N.N., 1997. Experimental study of dissociation of HCl from 350 to 500°C and from 500 to 2500 bars: Thermodynamic properties of HCl°(aq). Geochim. Cosmochim. Acta 61, 4267–4280.

Ulrich, T., Günther, D., Heinrich, C.A., 1999. Gold concentrations of magmatic brines and the metal budget of porphyry copper deposits. Nature 399, 676–679.

Vasyukova, O.V., Williams-Jones, A.E., 2018. Direct measurement of metal concentrations in fluid inclusions, a tale of hydrothermal alteration and REE ore formation from Strange Lake, Canada. Chem. Geol. 483, 385–396.

Wang, R.C., Fontan, F., Chen, X.M., Hu, H., Liu, C.S., Xu, S.J., de Parseval, P., 2003. Accessory minerals in the Xihuashan Y-enriched granitic complex, southern China: a record of magmatic and hydrothermal stages of evolution. Can. Mineral. 41, 727–748.

Wang, X., Qiu, Y., Lu, J., Chou, I.M., Zhang, W., Li, G., Hu, W., Li, Z., Zhong, R., 2020. In situ Raman spectroscopic investigation of the hydrothermal speciation of tungsten: Implications for the ore-forming process. Chem. Geol. 532, 119299.

Wang, X.-S., Timofeev, A., Williams-Jones, A.E., Shang, L.-B., Bi, X.-W., 2019. An experimental study of the solubility and speciation of tungsten in NaCl-bearing aqueous solutions at 250, 300, and 350 °C. Geochim. Cosmochim. Acta 265, 313–329.

Wang, X.-S., Williams-Jones, A.E., Hu, R.-Z., Shang, L.-B., Bi, X.-W., 2021. The role of fluorine in granite-related hydrothermal tungsten ore genesis: Results of experiments and modeling. Geochim. Cosmochim. Acta 292, 170–187.

Webster, J.D., Thomas, R., Rhede, D., Förster, H.-J., Seltmann, R., 1997. Melt inclusions in quartz from an evolved peraluminous pegmatite: Geochemical evidence for strong tin enrichment in fluorine-rich and phosphorus-rich residual liquids. Geochim. Cosmochim. Acta 61, 2589–2604.

Wei, W., Hu, R., Bi, X., Peng, J., Su, W., Song, S., Shi, S., 2012. Infrared microthermometric and stable isotopic study of fluid inclusions in wolframite at the Xihuashan tungsten deposit, Jiangxi province. China. Miner. Depos. 47, 589–605.

Wesolowski, D., Drummond, S.E., Mesmer, R.E., Ohmoto, H., 1984. Hydrolysis equilibria of tungsten(VI) in aqueous sodium-chloride solutions to 300 °C: Inorganic Chemistry. Inorg. Chem. 23, 1120–1132.

Williams-Jones, A., Migdisov, A., 2014. Experimental constraints on the transport and deposition of metals in ore-forming hydrothermal systems. Soc. Econ. Geol. 18, 77–96.

Williams-Jones, A.E., Seward, T.M., 1989. The stability of calcium chloride ion pairs in aqueous solutions at temperatures between 100 and 360°C. Geochim. Cosmochim. Acta 53, 313–318.

Wood, S.A., Samson, I.M., 2000. The Hydrothermal Geochemistry of Tungsten in Granitoid Environments: I. Relative Solubilities of Ferberite and Scheelite as a Function of T, P, pH, and mNaCl. Econ. Geol. 95, 143–182.

Wu, M.Q., Samson, I.M., Zhang, D.H., 2017. Textural and Chemical Constraints on the Formation of Disseminated Granite-hosted W-Ta-Nb Mineralization at the Dajishan Deposit, Nanling Range, Southeastern China. Econ. Geol. 112, 855–887.

Xiang, L., Wang, R., Romer, R.L., Che, X., Hu, H., Xie, L., Tian, D., 2020. Neoproterozoic Nb-Ta-W-Sn bearing tourmaline leucogranite in the western part of Jiangnan Orogen: Implications for episodic mineralization in South China. Lithos 360–361, 105450.

Xie, G., Mao, J., Li, W., Fu, B., Zhang, Z., 2019. Granite-related Yangjiashan tungsten deposit, southern China. Miner. Depos. 54, 67–80.

Xie, L., Wang, R.-C., Che, X.-D., Huang, F.-F., Erdmann, S., Zhang, W.-L., 2016. Tracking magmatic and hydrothermal Nb–Ta–W–Sn fractionation using mineral textures and composition: A case study from the late Cretaceous Jiepailing ore district in the Nanling Range in South China. Ore Geol. Rev. 78, 300–321.

Xie, L., Wang, Z., Wang, R., Zhu, J., Che, X., Gao, J., Zhao, X., 2018. Mineralogical constraints on the genesis of W-Nb–Ta mineralization in the Laiziling granite (Xianghualing district, south China). Ore Geol. Rev. 95, 695–712.

Xie, L., Tao, X., Wang, R., Wu, F., Liu, C., Liu, X., Li, X., Zhang, R., 2020. Highly fractionated leucogranites in the eastern Himalayan Cuonadong dome and related magmatic Be–Nb–Ta and hydrothermal Be–W–Sn mineralization. Lithos 354–355, 105286.

Yang, J.-H., Zhang, Z., Peng, J.-T., Liu, L., Leng, C.-B., 2019. Metal source and wolframite precipitation process at the Xihuashan tungsten deposit, South China: Insights from mineralogy, fluid inclusion and stable isotope. Ore Geol. Rev. 111, 102965.

Zajacz, Z., Halter, W.E., Pettke, T., Guillong, M., 2008. Determination of fluid/melt partition coefficients by LA-ICPMS analysis of co-existing fluid and silicate melt inclusions: Controls on element partitioning. Geochim. Cosmochim. Acta 72, 2169–2197.

Zhan, Q., Gao, X.-Y., Meng, L., Zhao, T.-P., 2021. Ore genesis and fluid evolution of the Sandaozhuang supergiant W-Mo skarn deposit, southern margin of the North China Craton: Insights from scheelite, garnet and clinopyroxene geochemistry. Ore Geol. Rev. 139, 104551.

Zimmer, K., Zhang, Y., Lu, P., Chen, Y., Zhang, G., Dalkilic, M., Zhu, C., 2016. SUPCRTBL: A revised and extended thermodynamic dataset and software package of SUPCRT92. Comput. Geosci. 90, 97–111.